From complex magnetism ordering to simple ferromagnetism in two-dimensional LaCrSb_{3} by hole doping

Haijie Chen, Awadhesh Narayan, Lei Fang, Nicholas P. Calta, Fengyuan Shi, Duck Young Chung, Lucas K. Wagner, Wai-Kwong Kwok, and Mercouri G. Kanatzidis

Phys. Rev. B **94**, 134411 — Published 11 October 2016

DOI: 10.1103/PhysRevB.94.134411

From Complex Magnetism Ordering to Simple Ferromagnetism in the Two-dimensional $LaCrSb_3$ by Hole-doping

Haijie Chen,[†,§] Awadhesh Narayan,[∥] Lei Fang,[†,§] Nicholas P. Calta,[†] Fengyuan Shi,[‡] Duck Young Chung,[§] Lucas K. Wagner,[∥] Wai-Kwong Kwok,[§] and Mercouri G. Kanatzidis*[,†,‡,§]

[†]*Department of Chemistry, and* [‡]*Department of Materials Science and Engineering, Northwestern University, Evanston, Illinois 60208, United States*

[§]*Materials Science Division, Argonne National Laboratory, Argonne, Illinois 60439, United States*

[∥]*Department of Physics, University of Illinois at Urbana-Champaign, Illinois 61801, United States*

*Corresponding Author Email: m-kanatzidis@northwestern.edu

Abstract: Competing orders widely exist in many material systems, such as superconductivity, magnetism, and ferroelectricity. $LaCrSb_3$ is a highly anisotropic magnetic material in which the spins are aligned ferromagnetically (FM) in one direction and canted antiferromagnetically (AFM) in another in the Cr-Sb chains. Hole-doping with Sr^{2+} and Ca^{2+} in the La site suppresses the AFM correlations and transforms the anisotropic magnetic order into a FM lattice in all directions. First-principles density functional theory calculations show that the canted magnetic order becomes energetically less favorable compared to the FM order upon hole doping. Doping in the La site is an effective approach to modulate the competing orders in $LaCrSb_3$.

PACS number(s): 75.50.Cc, 75.50.Ee, 75.30.Cr, 75.30.Gw

Introduction

Materials with competing orders are of broad interest because they can lead to novel physical phenomena such as high temperature superconductivity [1−3], colossal magnetoresistance [4], and ferroelectricity [5−7]. Tuning and controlling competing orders are of high importance for understanding materials properties as well as for potential applications. For example, in the iron-based pnictides, both spin density wave and superconductivity exist in the phase diagram [3,8−10], antiferromagnetic (AFM) fluctuations are associated with superconductivity in heavy fermion compounds [2,11−13], and ferromagnetism (FM) and AFM compete in colossal magnetoresistance systems [4,14,15]. Often, these situations occur in materials with low dimensional structures.

In order to explore the presence of FM and AFM competing orders, we focused on $LaCrSb_3$ because of its two dimensional structure, unusual magnetic coupling behavior of the Cr atoms and the presence of a flat perfect square net of Sb atoms in the structure; the latter of which may be a source of density wave behavior [16−23]. *RE*$CrSb_3$ (*RE* = rare earth metals), a series of ternary intermetallic rare earth chromium antimonides, have rich and perplexing magnetic orderings [24−30]. $LaCrSb_3$, an archetypal compound of the *RE*$CrSb_3$ series, has a rich magnetic phase diagram and relative simplicity in magnetic nature due to the absence of 4*f* electrons in La^{3+} [31−35]. Below ~ 95 K, the spins are ordered ferromagnetically in the *b* direction and canted antiferromagnetically in the *c* direction [34]. Previous studies have suggested that AFM has an itinerant nature [31,33], while more detailed studies show that the localized Cr spins also contributes to the magnetic behavior [34]. Partial substitution of Cr by other elements suppresses the AFM long range order [32,35]. However, the FM is also suppressed as a result of doping in

the Cr site. Doping with other magnetic rare-earth elements in the La site has shown an even more complicated magnetic phase diagram [29].

In $LaCrSb_3$, we aim to induce a substantial lowering of the Fermi energy in order to investigate the effects of magnetic coupling on Cr to probe for competing states. Our approach focuses on doping the La atom sublattice with aliovalent elements (such as Sr^{2+} and Ca^{2+}) to achieve "oxidation" on the Cr-Sb chain structure. Doping the La site with alkaline earth 2+ ions does not cause substitutional disorder on the magnetic Cr sublattice nor on the square net Sb sublattice. Instead of combined FM and AFM orders, a simple FM lattice is observed. Our density functional theory calculations are in qualitative agreement with our experimental findings, and show that the canted magnetic order becomes energetically less favorable compared to FM order upon hole doping.

Results and Discussion

Synthesis and Structure. The structure of $LaCrSb_3$ as shown in Fig. 1(a) consists of Cr-Sb layers and Sb square nets separated by La^{3+} cations along the *a* axis. The Cr-Sb layer is formed by face-sharing $CrSb_6$ octahedra and extended along the *bc* plane. Fig. 1(b) shows the spin-canting in pristine $LaCrSb_3$ which leads to emergence of AFM < 95 K [34]. The canted spin arrangement generates opposite spin polarity in the *c* axis, forming an AFM exchange interaction.

To successfully introduce Sr or Ca in the structure of $LaCrSb_3$, a large excess of alkaline earth metals was used. The molar ratio of [Sr, Ca] to La needs to be greater than one. However, when the [Sr, Ca]/La molar ratio was >2.5, no single crystals were obtained. Below this ratio, the obtained single crystals were pure $LaCrSb_3$ (Fig. 1S) [36]. For higher dopant concentrations, both Ca^{2+} and Sr^{2+} successfully dope $LaCrSb_3$ on the La site, as confirmed by energy dispersive X-ray spectroscopy and scanning electron microscopy (SEM/EDS) (Figs. 2S and 3S) [36]. For the Sr^{2+} doped crystals, the actual doping level *x* was found to vary from 0.05 to 0.15, and for the Ca^{2+} doped crystals, between 0.15 and 0.60. The plate-like single crystals display shiny metallic-color with typical dimensions of ~ 0.1 mm × 0.5 mm × 0.02 mm (Figs. 1(c) and 1(d)).

For accuracy, single-crystal structures of $La_{1-x}Sr_xCrSb_3$ and $La_{1-x}Ca_xCrSb_3$ were determined using X-ray diffraction at room temperature (293 K). The crystallographic data and structural refinements for samples with the highest doping level are listed in Table I. The results for samples with other doping levels are listed in Table 1S–4S [36]. All of the compounds crystallize in the same orthorhombic space group *Pbcm*. For $LaCrSb_3$, the unit cell parameters are a = 13.274(3) Å, b = 6.2028(12) Å and c = 6.1086(12) Å, which are slightly smaller than previously reported data (a = 13.2835(7) Å, b = 6.2127(2) Å and c = 6.116 (1) Å) [24]. Fractional atomic coordinates and thermal displacement parameters (U_{eq})

for $La_{1-x}Sr_xCrSb_3$ and $La_{1-x}Ca_xCrSb_3$ are listed in Tables 5S and 6S, respectively [36]. Anisotropic displacement parameters are presented in Tables 7S and 8S [36].

For $La_{1-x}Sr_xCrSb_3$, refined X-ray diffraction gives x = 0, 0.05(8), 0.08(3), and 0.16(3), in agreement with the SEM/EDS results. The determined lattice parameters increase with higher doping levels generating larger cell volumes, consistent with the introduction of the larger Sr^{2+} ion into the La site in $LaCrSb_3$. The higher doping level for $La_{1-x}Ca_xCrSb_3$ with x = 0.14(1), 0.31(3), and 0.62(3) indicates that the smaller Ca^{2+} ion substitutes La^{3+} more easily in the $LaCrSb_3$ system.

Charge Transport. The electrical resistivity of $La_{1-x}Sr_xCrSb_3$ (x = 0, 0.05(8), 0.08(3), 0.16(3)) and $La_{1-x}Ca_xCrSb_3$ (x = 0, 0.14(1), 0.31(3), 0.62(3)), as measured along the c axis of single crystal samples, are shown in Figs. 2(a) and 2(b), respectively. The electrical resistivity decreases upon cooling for all measured samples, indicative of metallic behavior. The introduction of Sr^{2+} and Ca^{2+} decreases the resistivity. For $La_{1-x}Sr_xCrSb_3$ (x = 0, 0.05(8), 0.08(3), 0.16(3)) and $La_{1-x}Ca_xCrSb_3$ (x = 0, 0.14(1), 0.31(3), 0.62(3)), the resistivity decreases from 85 μΩ cm to 45 μΩ cm and from 85 μΩ cm to 14 μΩ cm, respectively. All of the data show a slight drop at around 130 K, which may be due to reduced electron-spin scattering below the ferromagnetic transition [33]. As plotted in Fig. 2(c), the introduction of neither Sr^{2+} nor Ca^{2+} causes the anomaly to shift, indicating that the Curie temperature (T_c) is almost identical for all samples. The magnetic transition in undoped $LaCrSb_3$ is due to the Cr 3d electrons [33]. Considering that Cr^{3+} is the only magnetic ion in this system, it is reasonable that the doping of the La site with some Sr^{2+} and Ca^{2+} does not change the T_c. As displayed in Figs. 4S and 5S, the resistivity decreases linearly with T above the transition temperature and as $T^{3/2}$ below it, which is typical for FM systems [36, 37].

The Hall effect was measured to probe the conducting carriers. Considering that both Sr^{2+} and Ca^{2+} are expected to act as acceptors and induce hole-doping, we investigated two

samples, $LaCrSb_3$ and $La_{0.83(7)}Sr_{0.16(3)}CrSb_3$. The Hall resistivity $R_{xy} = [R(+H) - R(-H)]/2$ was obtained by switching the magnetic field at each point to reduce the effect of Hall electrode misalignment. R_{xy} versus magnetic field $\mu_0 H$ at different temperatures for $LaCrSb_3$ and $La_{0.83(7)}Sr_{0.16(3)}CrSb_3$ are shown in Figs. 6S and 7S, respectively [36]. The calculated temperature-dependent carrier density (n) is presented in Fig. 2(d). The inset shows the linear field dependence of the Hall resistivity at 300 K. The positive R_{xy} indicates that the dominant charge carriers are holes in both $LaCrSb_3$ and $La_{0.83(7)}Sr_{0.16(3)}CrSb_3$ as expected. R_{xy} decreases linearly with decreasing magnetic field. The temperature dependent variance in both samples shows similar behavior. For $LaCrSb_3$, the hole carrier concentration n (~ 2.4×10^{22} cm^{-3}) decreases with decreasing temperature until T=150 K (~ 1.1×10^{22} cm^{-3}). Below 150 K, n increases as the temperature decreases further (~ 2.1×10^{22} cm^{-3} at 5 K). For $La_{0.83(7)}Sr_{0.16(3)}CrSb_3$, n varies as ~ 5.1×10^{22} cm^{-3} at 300 K, ~ 1.1×10^{22} cm^{-3} at 150 K and ~ 2.1×10^{22} cm^{-3} at 5 K. The increased carrier concentration for the hole doped $La_{0.83(7)}Sr_{0.16(3)}CrSb_3$ confirms the hole doping and the resultant decrease of the resistivity. Earlier studies on charge transport properties of $LaCrSb_3$ also reported its hole-type behavior, which could be attributed to double-exchange interaction in the Cr-Sb chains [34,38]. The calculated mobility at 300 K of doped $La_{0.83(7)}Sr_{0.16(3)}CrSb_3$ is ~ 2.7 $cm^2V^{-1}s^{-1}$ which is slightly smaller than that of $LaCrSb_3$ (~ 3.1 $cm^2V^{-1}s^{-1}$). Introduction of dopants in the La site seems to have a minor effect on the mobility.

Magnetization. The magnetization as a function of field (0 – 2 T) at 5 K along the a, b and c axes for $LaCrSb_3$, $La_{0.83(7)}Sr_{0.16(3)}CrSb_3$, and $La_{0.37(7)}Ca_{0.62(3)}CrSb_3$ are shown in Figs. 3(a), 3(b), and 3(c), respectively. Further magnetization at small magnetic field (0 – 5 kOe) is shown in Fig. 8S. The magnetization shows highly anisotropic behavior along the different directions. In all three compounds, the magnetization along the b axis saturates almost

immediately with applied field. The magnetization along the *c* axis saturates at higher fields to magnetization values close to that of the *b* axis. In contrast, the magnetization along the *a* axis increases linearly with increasing field with no evidence of saturation. The magnetization behavior along the *b* and *a* axes for the Sr^{2+} and Ca^{2+} doped samples is similar to that of pristine $LaCrSb_3$. For the data along the *c* axis, the bump present in $LaCrSb_3$ at around 0.2 T, which is due to the AFM ordering along the *c* axis [33], disappears in the doped samples. This implies that in the doped samples the AFM order is suppressed.

The 1000 Oe field-cooled (FC) magnetization vs temperature curves (M-T) along the *a*, *b* and *c* axes for $LaCrSb_3$, $La_{0.83(7)}Sr_{0.16(3)}CrSb_3$, and $La_{0.37(7)}Ca_{0.62(3)}CrSb_3$ is shown in Figs. 3(d), 3(e) and 3(f), respectively. It is clear that the AFM in $LaCrSb_3$ is suppressed as a result of Sr^{2+} or Ca^{2+} doping and the system transforms into a pure FM material, which is further confirmed by the 10 Oe FC M-T results in Fig. 8S [36]. Figs. 9S and 10S summarize the temperature dependence magnetization for all samples with different doping levels along the *b* axis [36]. The introduction of Sr^{2+} and Ca^{2+} leads to minor increased moment. For $LaCrSb_3$, the magnetization along the *b* axis at 5 K is 1.19 μ_B/formula unit (μ_B/f.u.). For $La_{0.83(7)}Sr_{0.16(3)}CrSb_3$, and $La_{0.37(7)}Ca_{0.62(3)}CrSb_3$, this value increases to 1.39 μ_B/f.u. and 1.58 μ_B/f.u., respectively. The FM transition temperature remains at around 130 K for all systems, consistent with the resistivity results.

Calculations and Analysis. We want to understand two main effects seen in our experiments. First, the ground state changes upon hole doping, and second, the T_c does not change. To understand these features, we considered several ferromagnetic (FM) and antiferromagnetic (AFM) configurations: FM-(*a*,*b*,*c*), AFM-*c*, and FM-canted. Here (*a*,*b*,*c*) denote the crystal axes along which the magnetic moments can point. In the FM-canted configuration, the magnetic moments are canted ~ 18° from the *b* axis. Out of these AFM-*c*

and FM-canted are seen in experiment, along with FM-*b*. We also considered FM-*a* and FM-*c* to check if we find the right easy-axis for the ground state in our calculations.

We carried out density functional theory (DFT) calculations using the Elk code [39] including spin-orbit coupling via the second variational formulation. We used the Perdew-Burke-Ernzerhof (PBE) form of the exchange-correlation functional [40], with a basis cutoff $RG_{\max}$ of 8.0 and a *k*-point grid of 4 × 8 × 8. Fermi surfaces were plotted using XCrySDen [41]. We note that treatment of disorder in this framework including spin-orbit coupling is computationally prohibitively expensive.

The density of states for experimentally observed magnetic configurations, FM-*b*, AFM-*c* and FM-canted are shown in Fig. 4. In all cases, the predominant contribution at the Fermi level comes from Cr states. The main effect of doping is a shift of about ~0.08 eV for most of the features in the DOS for these magnetic configurations. The magnetic moment for both undoped and doped systems is close to 2 μ_B in the different studied FM configurations. For FM-*b* configuration, the magnetic moment reduces from 2.07 μ_B to 2.01 μ_B upon doping, while for FM-canted configuration it decreases from 2.11 μ_B to 1.98 μ_B. We also show, in Fig. 5, the evolution of Fermi surfaces with doping. Different colors represent different bands crossing the Fermi level. For the two FM configurations, the main effect of hole doping is to enlarge the central hole pocket, shown in yellow, which has significant Cr contribution. By estimating the change in volume of this hole pocket we found the change in hole density to be $\sim 0.7 \times 10^{22}$ cm^{-3}, which is the same order of magnitude value as the experimental estimate.

Table II contains a summary of the energies of different magnetic configurations. If one were to estimate the energy scale of exchange coupling from these energies, it would result in a T_c smaller than that experimentally observed. This could either be due to errors in the PBE functional, which can underestimate magnetic energy differences [42] or could be due to the Heisenberg model not providing an appropriate description of this system. Within DFT-PBE,

we always find that the FM-*b* magnetic ordering is lowest in energy, although for the undoped case, the experimental configuration FM-canted is very close in energy by 0.22 meV. On hole doping, the FM-canted configuration becomes less stable, i.e. it becomes higher in energy compared to FM-*b*, reproducing the trend seen in our experiments. Sb atoms contribute substantially to the spin-orbit energy and we find that upon doping the occupation of Sb atoms changes by about 0.25 electrons per unit cell. This change in occupation may therefore tip over the fine balance between the relative stability of FM-canted and FM-*b* magnetic configurations. This is a likely reason why we can control the relative energy of the two FM configurations using doping.

So, to summarize, from our first-principles calculations we find results which are qualitatively in agreement with experiments, in that: (i) the canted order becomes less stable with doping, (ii) FM-*b* is the most stable FM structure, and (iii) the magnetic moment is similar to the experimental value for both doped and undoped compounds. Overall, the calculations support our experimental interpretation that the introduction of holes into the system can control the magnetic ordering in $LaCrSb_3$, potentially via changing the occupation of the Sb atoms.

Conclusion

In order to tune and control the complex FM and AFM orders in $LaCrSb_3$, doping in the La site was designed and successfully realized. Our studies demonstrate that hole-doping in the highly anisotropic magnetic material $LaCrSb_3$ can effectively suppress the AFM spin canting order and transform the magnetic complexity into simple a FM lattice. Our first-principles density functional theory calculations show that the canted magnetic order

becomes energetically less favorable compared to the FM order upon hole doping. Our studies reveal an effective mean to tune competing orders in $LaCrSb_3$.

Acknowledgements

This work was supported as part of the Center for Emergent Superconductivity, an Energy Frontier Research Center funded by the U.S. Department of Energy, Office of Science, Office of Basic Energy Sciences. Computational resources were provided by the University of Illinois Campus Cluster. This work made use of the EPIC facility of the NU*ANCE* Center at Northwestern University, which has received support from the Soft and Hybrid Nanotechnology Experimental (SHyNE) Resource (NSF NNCI-1542205); the MRSEC program (NSF DMR-1121262) at the Materials Research Center; the International Institute for Nanotechnology (IIN); the Keck Foundation; and the State of Illinois, through the IIN.

References

[1] J. G. Bednorz, and K. A. Müller, Z. Phys. B **64**, 189 (1986).

[2] C. Petrovic, P. G. Pagliuso, M. F. Hundley, R. Movshovich, J. L. Sarrao, J. D. Thompson, Z. Fisk, and P. Monthoux, J. Phys.: Condens. Matter **13**, 337 (2001).

[3] Y. Kamihara, T. Watanabe, M. Hirano, and H. Hosono, J. Am. Chem. Soc. **130**, 3296 (2008).

[4] M. N. Baibich, J. M. Broto, A. Fert, F. Nguyen Van Dau, F. Petroff, P. Etienne, G. Creuzet, A. Friederich, and J. Chazelas, Phys. Rev. Lett. **61**, 2472 (1988).

[5] J. G. Bednorz, and K. A. Müller, Phys. Rev. Lett. **52**, 2289 (1984).

[6] S. Park, and T. R. Shrout, J. Appl. Phys. **82**, 1804 (1997).

[7] J. H. Haeni, P. Irvin, W. Chang, R. Uecker, P. Reiche, Y. L. Li, S. Choudhury, W. Tian, M. E. Hawley, B. Craigo, A. K. Tagantsev, X. Q. Pan, S. K. Streiffer, L. Q. Chen, S. W. Kirchoefer, J. Levy, and D. G. Schlom, Nature **430**, 758 (2004).

[8] H. Takahashi, K. Igawa, K. Arii, Y. Kamihara, M. Hirano, and H. Hosono, Nature **453**, 376 (2008).

[9] X. H. Chen, T. Wu, G. Wu, R. H. Liu, H. Chen, and D. F. Fang, Nature **453**, 761 (2008).

[10] M. Rotter, M. Tegel, and D. Johrendt, Phys. Rev. Lett. **101**, 107006 (2008).

[11] F. Steglich, J. Aarts, C. D. Bredl, W. Lieke, D. Meschede, W. Franz, and H. Schäfer, Phys. Rev. Lett. **43**, 1892 (1979).

[12] S. Friedemann, T. Westerkamp, M. Brando, N. Oeschler, S. Wirth, P. Gegenwart, C. Krellner, C. Geibel, and F. Steglich, Nat. Phys. **5**, 465 (2009).

[13] E. Schuberth, M. Tippmann, L. Steinke, S. Lausberg, A. Steppke, M. Brando, C. Krellner, C. Geibel, R. Yu, Q. M. Si, and F. Steglich, Science **351**, 485 (2016).

[14] R. M. Kusters, J. Singleton, D. A. Keen, R. McGreevy, and W. Hayes, Phys. B: Condens. Matter **155**, 362 (1989).

[15] K. I. Chahara, T. Ohno, M. Kasai, and Y. Kozono, Appl. Phys. Lett. **63**, 1990 (1993).

[16] X. Zhang, J. Li, B. Foran, S. Lee, H. Y. Guo, T. Hogan, C. R. Kannewurf, and M. G. Kanatzidis, J. Am. Chem. Soc. **117**, 10513 (1995).

[17] V. Brouet, W. L. Yang, X. J. Zhou, Z. Hussain, N. Ru, K. Y. Shin, I. R. Fisher, and Z. X. Shen, Phys. Rev. Lett. **93**, 126405 (2004).

[18] K. Y. Shin, V. Brouet, N. Ru, Z. X. Shen, and I. R. Fisher, Phys. Rev. B **72**, 085132 (2005).

[19] C. Malliakas, S. J. L. Billinge, H. J. Kim, and M. G. Kanatzidis, J. Am. Chem. Soc. **127**, 6510 (2005).

[20] H. J. Kim, C. D. Malliakas, A. T. Tomic, S. H. Tessmer, M. G. Kanatzidis, and S. J. L. Billinge, Phys. Rev. Lett. **96**, 226401 (2006).

[21] M. A. Zhuravleva, M. Evain, V. Petricek, and M. G. Kanatzidis, J. Am. Chem. Soc. **129**, 3082 (2007).

[22] C. D. Malliakas and M. G. Kanatzidis, J. Am. Chem. Soc. **131**, 6896 (2009).

[23] H. M. Eiter, M. Lavagnini, R. Hackl, E. A. Nowadnick, A. F. Kemper, T. P. Devereaux, J. H. Chu, J. G. Analytis, I. R. Fisher and L. Degiorgi, Proc. Natl. Acad. Sci. USA **110**, 64 (2013).

[24] M. J. Ferguson, R. W. Hushagen, and A. Mar, J. Alloys Compd. **249**, 191 (1997).

[25] M. L. Leonard, I. S. Dubenko, and N. Ali, J. Alloys Compd. **303**, 265 (2000).

[26] L. Deakin, M. J. Ferguson, A. Mar, J. E. Greedan, and A. S. Wills, Chem. Mater. **13**, 1407 (2001).

[27] L. Deakin, and A. Mar, Chem. Mater. **15**, 3343 (2003).

[28] S. J. Crerar, L. Deakin, and A. Mar, Chem. Mater. **17**, 2780 (2005).

[29] D. D. Jackson, and Z. Fisk, Phys. Rev. B **73**, 024421 (2006).

[30] M. Inamdar, A. Thamizhavel, and S. Ramakrishnan, J. Magn. Magn. Mater. **320**, 2766 (2008).

[31] N. Raju, J. E. Greedan, M. J. Ferguson, and A. Mar, Chem. Mater. **10**, 3630 (1998).

[32] I. S. Dubenko, P. Hill, and N. Ali, J. Appl. Phys. **89**, 7362 (2001).

[33] D. D. Jackson, M. Torelli, and Z. Fisk, Phys. Rev. B **65**, 014421 (2001).

[34] E. Granado, H. Martinho, M. S. Sercheli, P. G. Pagliuso, D. D. Jackson, M. Torelli, J. W. Lynn, C. Rettori, Z. Fisk, and S. B. Oseroff, Phys. Rev. Lett. **89**, 107204 (2002).

[35] X. Lin, V. Taufour, S. L. Bud'ko, and P. C. Canfield, Philo. Mag. **94**, 1277 (2014).

[36] See Supplemental Material at [*URL will be inserted by publisher*] for details of the experimental details, energy dispersive spectrum, resistivity analysis, Hall resistivity, magnetization at small magnetic field and structure refinements of compounds with other doping levels.

[37] N. Rivier, and A. E. Mensah, Phys. B+C **91**, 85 (1977).

[38] T. Hoang, and D. Jackson, APS March Meeting, March 21–25 Abstracts *(*2005).

[39] http://elk.sourceforge.net

[40] J.P. Perdew, K. Burke, and M. Ernzerhof, Phys. Rev. Lett. **77**, 3865 (1996).

[41] A. Kokalj, Comp. Mater. Sci., **28**, 155 (2003).

[42] B. Busemeyer et al., Phys. Rev. B **94**, 035108 (2016).

Figures and Tables

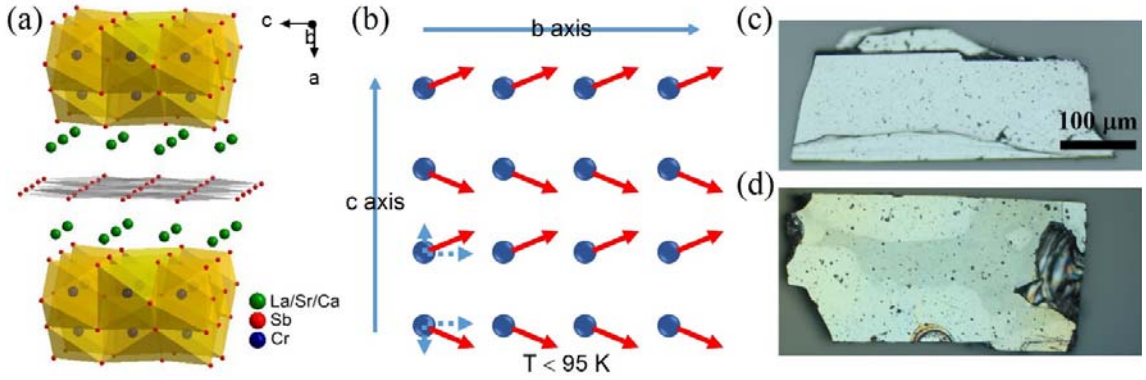

FIG. 1. (a) Crystal structure of $LaCrSb_3$ as viewed along the *b* axis. La (Sr, Ca), Cr, and Sb atoms are shown as green, blue, and red spheres, respectively. The planar Sb square net is grey labeled. (b) Projection of the Cr sublattice onto the *bc* plane. The arrows represent the Cr magnetic structures below 95 K [34]. Typical images of (c) $LaCrSb_3$ and (d) Ca-doped $LaCrSb_3$ single crystals with smooth surface.

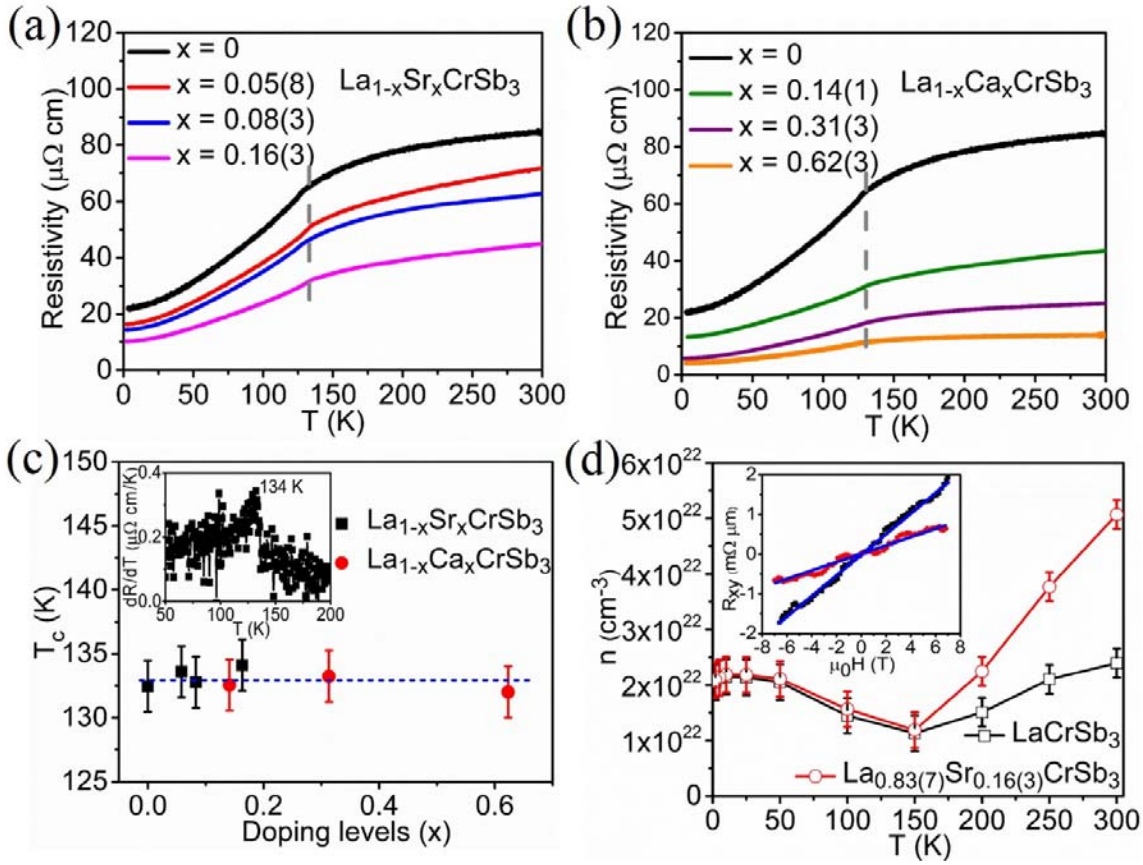

FIG. 2. Temperature-dependent resistivity along the *c* axis for (a) $La_{1-x}Sr_xCrSb_3$ (x = 0, 0.05(8), 0.08(3), 0.16(3)) and (b) $La_{1-x}Ca_xCrSb_3$ (x =0, 0.14(1), 0.31(3), 0.62(3)), respectively. (c) The determined Currie temperature (T_c) versus doping levels (x). Inset: determined T_c in $La_{0.83(7)}Sr_{0.16(3)}CrSb_3$ by temperature-dependent dR/dT. (d) Temperature-dependent carrier density (n). The inset is the room temperature Hall resistivity at 300 K which displays linear field dependence.

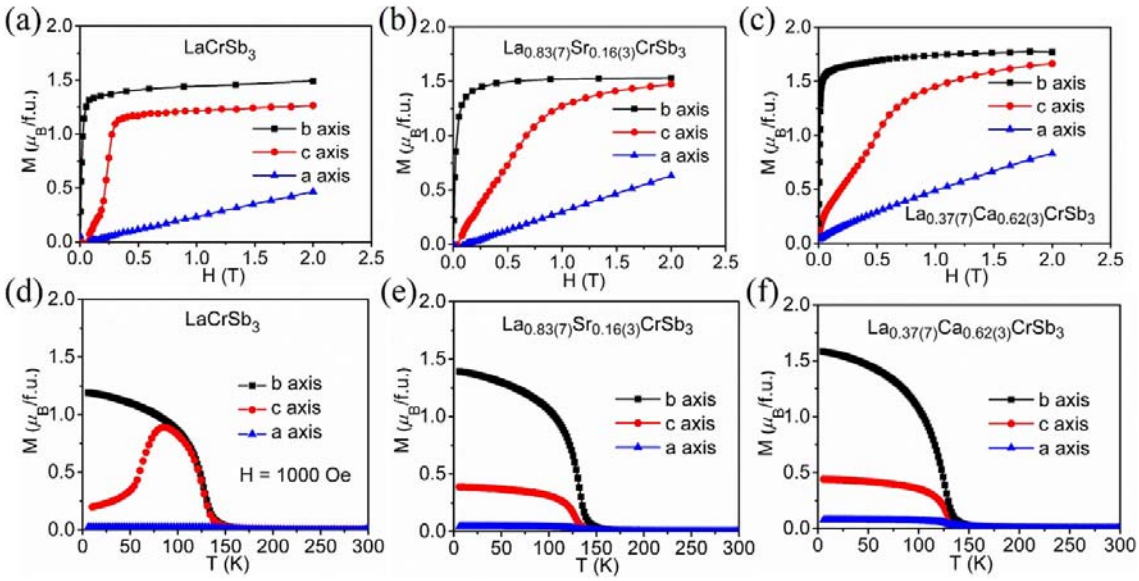

FIG. 3. Magnetization as a function of magnetic field at 5 K along the, *b* (black) and *c* (red), and *a* (blue) axes for (a) $LaCrSb_3$, (b) $La_{0.83(7)}Sr_{0.16(3)}CrSb_3$, and (c) $La_{0.37(7)}Ca_{0.62(3)}CrSb_3$. Temperature dependence of magnetization for (d) $LaCrSb_3$, (e) $La_{0.83(7)}Sr_{0.16(3)}CrSb_3$, and (f) $La_{0.37(7)}Ca_{0.62(3)}CrSb_3$ with an applied field of 1000 Oe under the field-cooled (FC) conditions (200 K – 5 K).

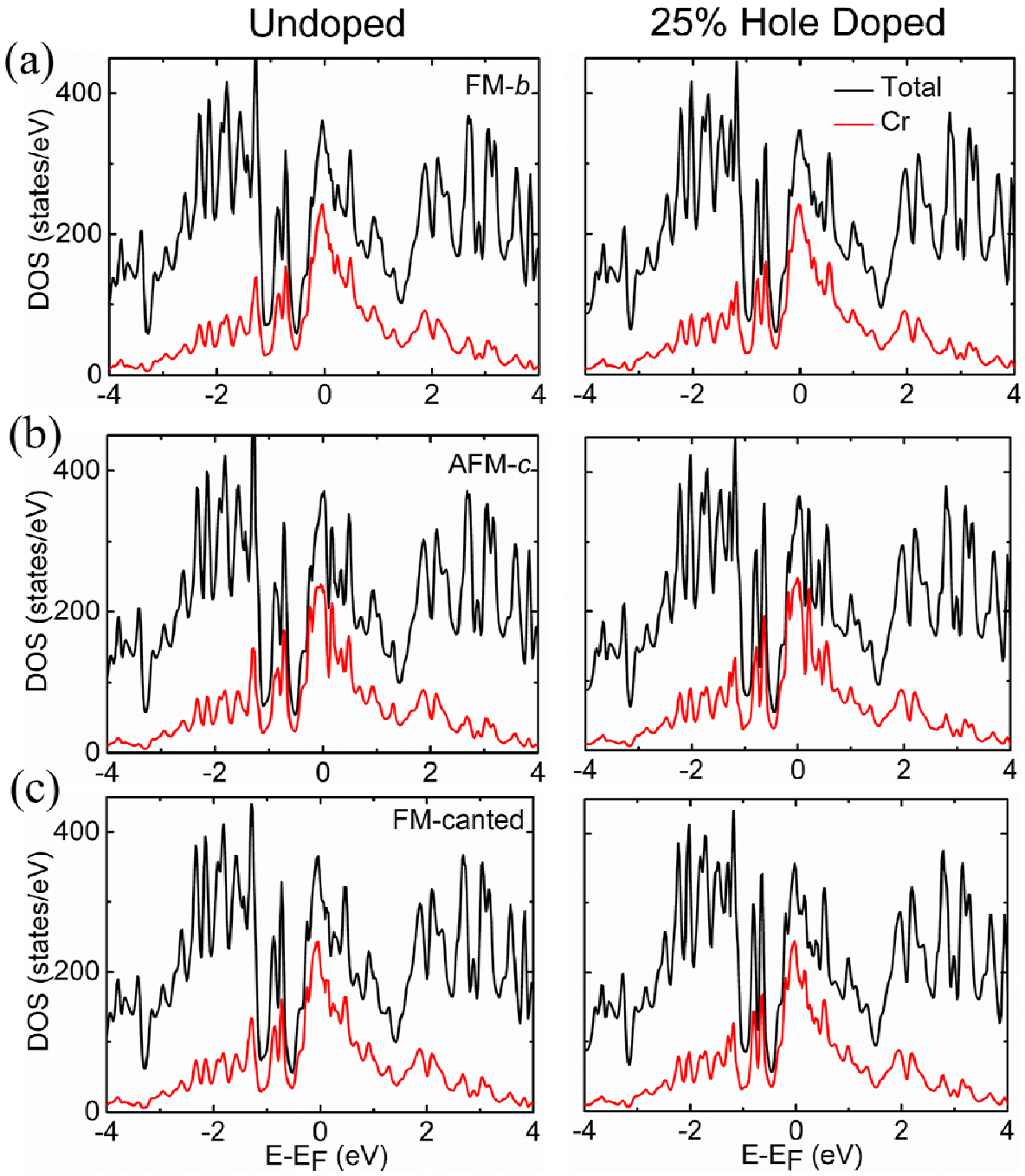

FIG. 4. Density of states for (a) FM-*b,* (b) AFM-*c* and (c) FM-canted magnetic configurations for undoped (left panel) and 25% hole doped systems (right panel).

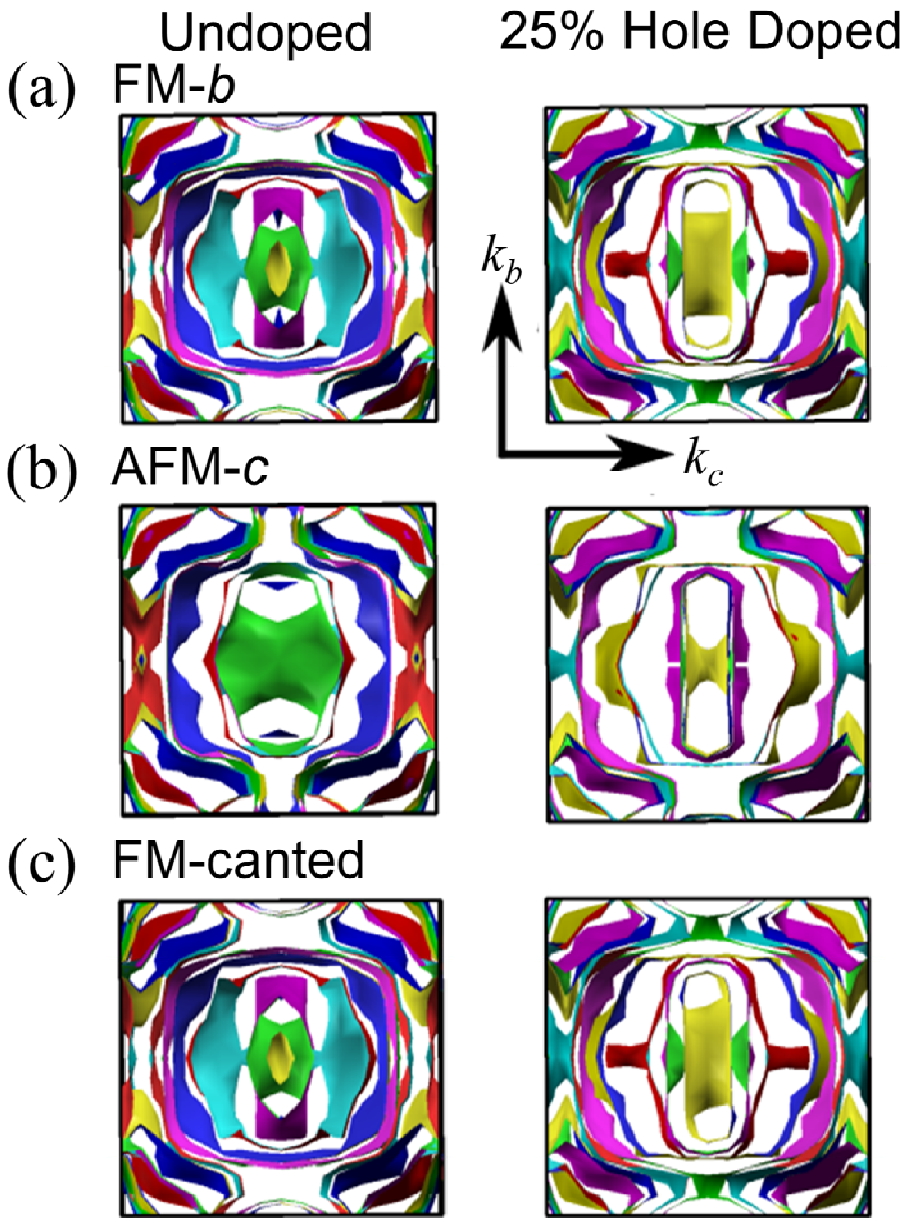

FIG. 5. Fermi surfaces for (a) FM-*b,* (b) AFM-*c* and (c) FM-canted magnetic configurations for undoped (left panel) and 25% hole doped systems (right panel).

Table I. Crystal data and structure refinements for $LaCrSb_3$, $La_{0.83(7)}Sr_{0.16(3)}CrSb_3$, and $La_{0.37(7)}Ca_{0.62(3)}CrSb_3$[a]

Empirical formula, Z	$LaCrSb_3$, 4	$La_{0.83(7)}Sr_{0.16(3)}CrSb_3$, 4	$La_{0.37(7)}Ca_{0.62(3)}CrSb_3$, 4
Formula weight	556.16	547.83	494.64
Crystal system		Orthorhombic	
Space group		*Pbcm*	
a (Å)	13.274(3)	13.336(3)	13.282(3)
b (Å)	6.2028(12)	6.2029(12)	6.1740(12)
c (Å)	6.1086(12)	6.1120(12)	6.0506(12)
Volume (Å^3)	502.97(17)	505.61(17)	496.18(17)
Calculated density (g/cm^3)	7.345	7.197	6.622
Absorption coefficient (mm^{-1})	26.117	26.340	21.903
F(000)	936	924	844
Crystal size (mm^3)	0.1080 × 0.0701 × 0.0202	0.0946 × 0.0483 × 0.0035	0.2114 × 0.1019 × 0.0239
θ range for data collection (deg)	3.07 to 29.13	1.53 to 29.14	3.07 to 29.19
Index ranges	$-18 \le h \le 18$ $-8 \le k \le 8$ $-8 \le l \le 8$	$-18 \le h \le 18$ $-8 \le k \le 8$ $-8 \le l \le 8$	$-17 \le h \le 18$ $-8 \le k \le 8$ $-8 \le l \le 8$
Reflections collected	4590	4572	4521
Independent reflections	740 [R_{int} = 0.0629]	746 [R_{int} = 0.0452]	737 [R_{int} = 0.0612]
Completeness	99.7% to θ = 29.13°	99.9% to θ = 29.14°	99.9% to θ = 29.19°
Refinement method		Full-matrix least-squares on F^2	
Data / restraints / parameters	740 / 0 / 30	746 / 0 / 31	737 / 0 / 31
Goodness-of-fit	1.155	1.149	1.176
Final R indices [>2σ(I)][b]	R_{obs} = 0.0326, wR_{obs} = 0.0725	R_{obs} = 0.0279, wR_{obs} = 0.0608	R_{obs} = 0.0360, wR_{obs} = 0.0763
R indices [all data] [b]	R_{all} = 0.0406, wR_{all} = 0.0749	R_{all} = 0.0365, wR_{all} = 0.0632	R_{all} = 0.0457, wR_{all} = 0.0789
Extinction coefficient	0.0150(7)	0.0036(3)	0.0019(3)
Largest diff. peak and hole (e·Å^{-3})	1.741 and -3.329	2.856 and -2.547	1.513 and -2.232

[a]For all structures, T = 293(2) K and λ = 0.71073 Å. [b]$R = \Sigma \, ||F_o| - |F_c|| / \Sigma \, |F_o|$, $wR = \{\Sigma \, [w(|F_o|^2 - |F_c|^2)^2] / \Sigma \, [w(|F_o|^4)]\}[44]^{1/2}$ and calcd $w = 1/[\sigma^2(F_o^2) + (A \times P)^2 + (B \times P)]$ where $P = (F_o^2 + 2F_c^2)/3$. For $LaCrSb_3$, A = 0.0434 and B = 0.0000. For $La_{0.83(7)}Sr_{0.16(3)}CrSb_3$, A = 0.0370 and B = 0.0000. For $La_{0.37(7)}Ca_{0.62(3)}CrSb_3$, A = 0.0345 and B = 3.6017.

Table II. Energy for different magnetic configurations. The energy of the ferromagnetic state with the spins pointing along the *b* axis is chosen as the reference. Ferromagnetic arrangement with spins pointing along *a* axis (FM-*a*), along *c* axis (FM-*c*), antiferromagnetic arrangement along *c* axis (AFM-*c*) and a ferromagnetic configuration with spins canted from *b* axis (FM-canted) are considered.

Magnetic Configuration	Energy undoped (meV)	Energy 25% hole doped (meV)
FM-*a*	1.25	3.16
FM-*b*	0	0
FM-*c*	0.54	2.17
FM-canted	0.22	1.43
AFM-*c*	2.19	3.17